Appl Phys B (2009) 95: 617–625
DOI 10.1007/s00340-009-3561-5

Applied Physics B
Lasers and Optics

Multiple-scattering speckle in holographic optical coherence imaging

K. Jeong · J.J. Turek · M.R. Melloch · D.D. Nolte

Received: 26 November 2008 / Revised version: 20 March 2009 / Published online: 7 May 2009

Abstract We investigate the effect of multiple scattering on the image quality of holographic optical coherence imaging, which is a full-field coherence-domain imaging form of optical coherence tomography. The speckle holograms from turbid media and from multicellular tumor spheroids are characterized by high-contrast speckle on a multiply-scattered background caused by channel cross-talk. We quantify the multiple-scattered light that is accepted by the holographic coherence gate, and identify a cross-over from single-scattered to multiple-scattered light beyond 15 to 20 optical thicknesses. Speckle reduction relies on vibrating diffusers and on fast adaptive holograms in photorefractive quantum well devices. The high anisotropy factor for tumor tissue reduces multiply-scattered light contributions for biomedical tumor imaging.

PACS 42.30.Wb · 42.30.Ms · 42.40.My

K. Jeong
Department of Physics and Chemistry, Korea Military Academy, Seoul 139-799, South Korea
e-mail: jeongk@kma.ac.kr

J.J. Turek
Department of Basic Medical Sciences, Purdue University, West Lafayette, IN 47907, USA

M.R. Melloch
School of Electrical and Computer Engineering, Purdue University, West Lafayette, IN 47907, USA

D.D. Nolte (✉)
Department of Physics, Purdue University, West Lafayette, IN 47907-2036, USA
e-mail: nolte@physics.purdue.edu
Fax: +1765-4940706

1 Introduction to speckle in optical coherence imaging

Coherence-domain imaging has become a well-established biomedical imaging technique applied to a wide range of applications [1]. The most mature technique of this class is optical coherence tomography (OCT), which uses rapid point-by-point scanning heterodyne detection for signal demodulation and computed reconstruction [2–5]. OCT has passed clinical trials and become part of the array of new medical imaging technologies in use in hospitals. Another approach in coherence-domain imaging is *en face* tomography with wide field of view [6, 7]. Alternatively, a full-field coherence-domain imaging approach that requires no computed reconstruction, providing direct images from coherence-gated depths, is holographic optical coherence imaging (OCI) in photorefractive media [8–11]. The most effective dynamic holographic devices are photorefractive quantum wells [12–16] because of their high refresh speed, which enables real-time speckle reduction techniques to be applied to coherent imaging. The quantum-well devices were used to detect the first coherence-gated holograms of living tissue [17–19], and the state of the art has advanced to Fourier-domain holographic recording with improved readout performance [20–22]. Other photorefractive materials have been used for depth-gating applications and imaging through turbid media [23–29], and digital holographic approaches also have been successful [30–33].

Despite the advantages of full-frame coherence imaging, the use of temporally- and spatially-coherent illumination creates significant speckle in holographic OCI images. The simultaneous illumination of multiple spatial channels in holographic OCI causes channel cross-talk from the scattering medium of tissue [34–36]. The channel cross-talk results from the mutual interferences among the channels. Structural speckle must be distinguished from multiple-scattering

channel cross-talk that arises from the residual coherence in multiply-scattered light. Structural speckle has advantages as a means of extracting dynamic information from the tissue, and this type of dynamic speckle has been used to measure cell motility [17, 22, 31].

Multiple-scattering channel cross-talk can be reduced by illuminating the tissue with reduced spatial coherence. The spatial coherence of the illuminating beam can be scrambled using a low-angle vibrating diffuser [10], while retaining the structural speckle. These considerations for channel cross-talk open the door for important contributions by holographic OCI to biomedical imaging. In this paper, we demonstrate reduction of channel cross-talk in holographic OCI imaging of living tissue.

2 Photorefractive quantum well OCI system

Holographic optical coherence imaging (OCI) uses short-coherence light to produce depth-gated images. The incident signal beam is reflected coherently from living tissue, and only the signal beam zero-path-matched with the reference beam produces interference fringes at the dynamic holographic film. The dynamic holographic film (PRQW device) converts photo-induced space-charge into holographic gratings, and depth-gated holographic images are projected on the diffracted beam. In this process, the dynamic holographic film acts as the coherent demodulator. Early research on holographic OCI was performed with image-domain holography, in which the holographic film was located at the image plane of the imaging optics. However, image-domain holographic OCI was limited in dynamic range by the background scattered from dust or other imperfections on the holographic film. We developed Fourier-domain holographic OCI to reduce background and improve image quality. Fourier-domain holography is performed with the PRQW at the Fourier plane. Fourier-domain holographic OCI becomes background-free in practice and opens the full dynamic range of the CCD camera for imaging into tissue [20, 21].

The experimental set-up for Fourier-domain OCI is shown in Fig. 1. A femtosecond mode-locked Ti:sapphire laser with 120 fs pulse duration and 100 MHz repetition rate was pumped by a diode laser, and the center wavelength of the mode-locked laser was tuned to the exciton peak wavelength (836 nm). The laser beam passed a first polarizing beam splitter (PBS) to produce the signal beam with vertical polarization and reference beam with horizontal polarization. The intensities of signal and reference beam were controlled by a neutral density filter and a half-wave plate in front of the PBS. The incident signal beam was scrambled by a vibrating (20 Hz) diffuser to reduce spatial coherence at the object plane by the lenses L1 and L2. The scrambled

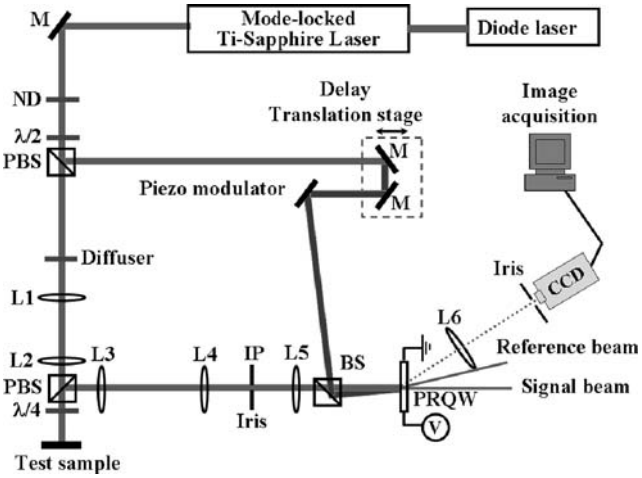

Fig. 1 Experimental set-up for Fourier-domain OCI: PBSs, polarizing beam splitter; BS, beam splitter; M's, mirrors; L1–L6, lenses; ND, neutral density filter; $\lambda/2$, half-wave plate; $\lambda/4$, quarter-wave plate; IP, image plane; PRQW, photorefractive quantum well; V, voltage

signal beam passed the second PBS and a quarter-wave plate behind the second PBS ensured that the backscattered signal beam had horizontal polarization after returning through the quarter-wave plate.

The backscattered beam was relayed with a 1:1 magnification by lenses L3 and L4. The lens L5 performed the Fourier transform of the signal beam, and the PRQW device was located at the Fourier plane. The signal beam interfered with the reference beam that passed through the delay stage. A vibrating mirror, which was controlled by a 20 Hz piezomodulator in the reference arm, was used to time-average interpixel laser speckle. Fringes from the interference between the signal and the reference beam were recorded on the PRQW device while a 10 kV/cm dc field was applied. The hologram was reconstructed by the $+1$ or -1 diffraction orders of the reference beam. The diffracted image was viewed through the 12-bit CCD camera by use of the lens L6. The reconstructed holographic images on the CCD camera were captured by a frame grabber in a computer. We used two PRQW devices in this study, with serial numbers PLO9 with a 3-mm window size, and JK1 with a 4-mm window size.

3 Dynamic range calibration

The first step of system calibration is the measurement of the depth resolution and sensitivity of the holographic OCI system. The round-trip FWHM of the source intensity coherence envelope was 26 μm measured by the electric field autocorrelation, as shown in Fig. 2(a). The depth resolution of the holographic OCI system is set by this value. To measure depth resolution and sensitivity, we used a 2.2 neutral

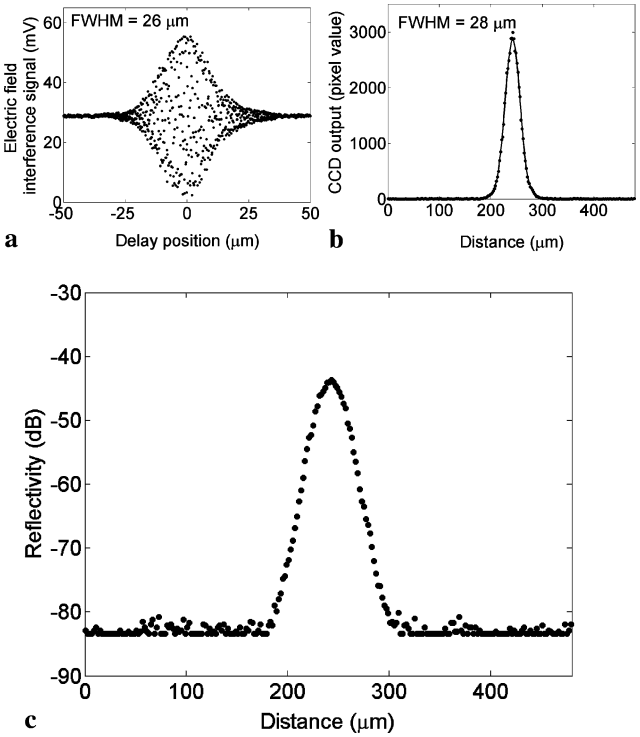

Fig. 2 (**a**) Electric field autocorrelation of the output of the laser beam with a FWHM of 26 μm incident on a mirror. (**b**) One pseudo A-scan from holographic *en face* images captured by the CCD camera with exposure time of 0.1 second. (**c**) Reflectivity as a function of depth showing the system sensitivity, which is calculated from (**b**)

density filter, followed by a mirror as the target. The target reflectivity was $-44\ \text{dB} = 20\log_{10} 10^{-2.2}$. Holographic images of the mirror were produced using a vibrating 5 degree diffuser and a computer-controlled reference delay with a depth step of 2 μm, captured to the CCD camera. Figure 2(b) shows the CCD output value of one pseudo A-scan (reflectance vs. depth) selected from holographic *en face* images. The incident signal intensity was 10 W/cm^2 at the target, and the exposure time of the CCD camera was 0.1 second. The measured depth resolution of the holographic OCI system was 28 μm from Fig. 2(b), which agrees with the FWHM of the electric field autocorrelation. Figure 2(c) shows the system sensitivity with the noise floor at -82 dB, which was extracted from Fig. 2(b). This demonstrates that the holographic OCI system with an incident intensity of 10 W/cm^2 with an exposure time of 0.1 second has a sensitivity of 82 dB.

In the second step of system calibration we identified speckle inside living tissue. The sample was an onion placed in water. Holographic images of the onion were captured by the CCD camera using a depth step of 10 μm step between frames. Figure 3 shows YZ cross sections of the holographic OCI images inside onion with the grayscale on a dB scale. When a vibrating diffuser was not used, the cross section showed high-contrast speckle, as shown in Fig. 3(a). When

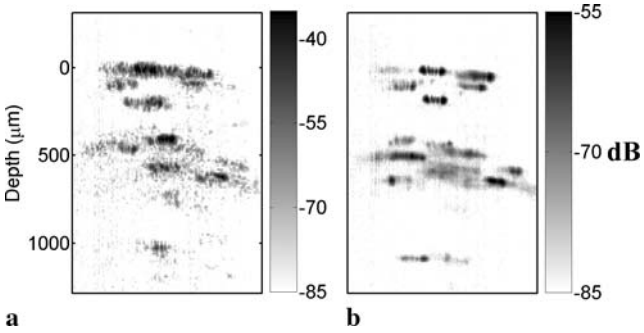

Fig. 3 YZ cross sections of holographic OCI images inside onion (**a**) without a diffuser and (**b**) with a vibrating 5 degree diffuser. The speckle in (**a**) was reduced by use of the vibrating diffuser

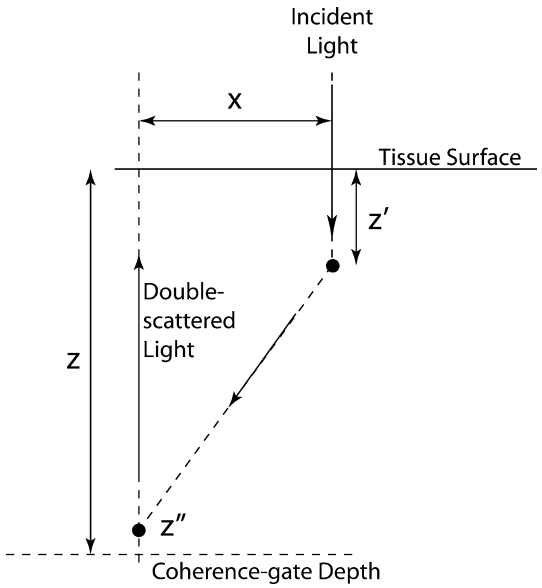

Fig. 4 Origin of multiple-scattering channel cross-talk in holographic OCI. The target is at depth z for single-scattered light. Many other paths that experience multiple scattering are path-matched to the coherence gate

a vibrating 5 degree diffuser was used in the OCI system, the speckle contrast in Fig. 3(a) was reduced, revealing uniform onion structure. Therefore, the holographic OCI system with a high-angle diffuser, such as a 5 degree diffuser, can be used to obtain the structure inside living tissue.

4 Multiple scattering

Multiple-scattering channel cross-talk results from the simultaneous illumination of multiple spatial channels in the scattering medium. Cross-talk occurs when multiply-scattered photons have the same optical path length as singly-scattered photons. This is illustrated in Fig. 4, in which a photon path that undergoes two scattering events has the same path length as a singly-scattered path. This co-

incidence allows a multiply-scattered photon to be accepted by the coherence gate that selects single-scattered photons from a selected depth. Multiple-scattering channel cross-talk results in a speckled coherent background that cannot be eliminated by the coherence gate and that degrades the image quality from the target depth.

Multiple scattering increases with depth, because there are more equal-path configurations possible with increasing depth in tissue. To illustrate this for double scattering in Fig. 4, consider a ray entering the surface of the tissue at position x. There are two scattering locations at z' and z'' that permit a path-matched ray to coincide with a single-scattered ray from the coherence depth at z. The path-matching condition is

$$2z = z' + z'' + \sqrt{x^2 + (z'' - z')^2}. \tag{1}$$

The deepest scattering location is set when $z'' = 0$, which gives

$$z'_{\max} = \frac{4z^2 - x^2}{4z}. \tag{2}$$

The total volume that can be accessed by double scattering is

$$V_2 = \int_0^{2z} 2\pi x \frac{4z^2 - x^2}{4z}\, dx = 2\pi z^3. \tag{3}$$

Therefore, the probability for double scattering being accepted into the coherence gate increases rapidly with the depth of the coherence gate. Although it is not easy to estimate is the depth beyond which multiple scattering dominates over single-scattered light, this can be determined empirically.

The relevant parameter to describe multiple scattering is the optical thickness $\tau = \mu' L$, where μ' is the reduced extinction coefficient and L is the optical path length. The reduced extinction coefficient is the sum of the absorption and reduced scattering coefficient. The depth for the cross-over between single scattering and multiple scattering can be different for different criteria and experimental methods. In coherence-gated transillumination imaging, the division point for ballistic and diffuse components, in which the ballistic component intensity becomes similar to the diffuse component intensity, was about 25 optical thickness [37].

To reduce multiple-scattering channel cross-talk in the holographic images, it is necessary to decrease the spatial coherence. Even though the number of photons with the same path length as a singly-scattered photon is not decreased with reduced spatial coherence, the photons accepted by the coherence gate is decreased. One method to accomplish this is to scramble the spatial coherence of the illumination, which is accomplished using a vibrating diffuser in the illumination beam and time-averaging on the CCD camera. The photorefractive quantum wells are particularly well suited for this technique because the holographic gratings are fast enough to track the moving holographic fringes [38], maintaining the diffraction efficiency even though the fringe velocity is high. The vibrating diffuser in the illumination beam does not affect the hologram formation in the fast photorefractive quantum wells, while time-averaging on the CCD camera homogenizes the speckle and reduces the background speckle contrast. This increases the image quality by increasing the ratio of the image intensity to the fluctuations of the background speckle.

To quantify the role of multiple scattering in the holographic OCI system, we performed multiple-scattering channel cross-talk experiments using white paper in water as the target. The schematic of the target is illustrated in Fig. 5(a). Paper with a thickness of 95 μm was placed in water between two microscope cover slips, each with 200 μm thickness. The gap between the cover slips was 155 μm and the incident illumination beam was scrambled using a vibrating 5 degree diffuser. The optic axis of the incident laser beam was positioned at the edge of the paper. The reduced extinction coefficient of the paper target was measured to be 125 mm^{-1}. The holographic images of the target were captured by the CCD camera using a depth step of 10 μm. Figure 5(b) shows a YZ cross section selected from the holographic images. The edge of the diffuse target is clearly identifiable. The horizontal features in the figure are from the surfaces of the microscope cover slips. The scattering from the paper (image grayscale is on a log scale) extends to the depth of 350 μm. Because the thickness of paper was 95 μm, it is clear that any signal beyond the depth of 95 μm results from multiple-scattering channel cross-talk.

Figure 5(c) shows 400 pseudo A-scans selected out of 250,000 from the holographic *en face* images. The pseudo A-scans were selected in the 32 by 32 μm^2 area of the diffuse paper. If there were no multiple-scattering channel cross-talk in the holographic images, the slope of pseudo A-scans should be a single exponential (straight line), such as the solid line in the figure. Therefore, the signal to the right of the dashed line (the limit of the paper target) in Fig. 5(c) is from multiple-scattering channel cross-talk, and becomes dominant beyond the depth of 50 μm. The optical thickness corresponding to the depth of 50 μm is 12.5 for the round-trip.

To investigate the reduction of multiple-scattering channel cross-talk by use of the vibrating diffuser, we produced *en face* images of uniform scattering media in the holographic OCI system with no diffuser and with a vibrating diffuser, respectively. The uniform scattering medium was 0.5-μm diameter polystyrene beads in water between two microscope cover slips. The reduced extinction coefficient of this medium was measured to be 55 mm^{-1}. Figures 6(a) and (b) show pseudo A-scans selected from the holographic

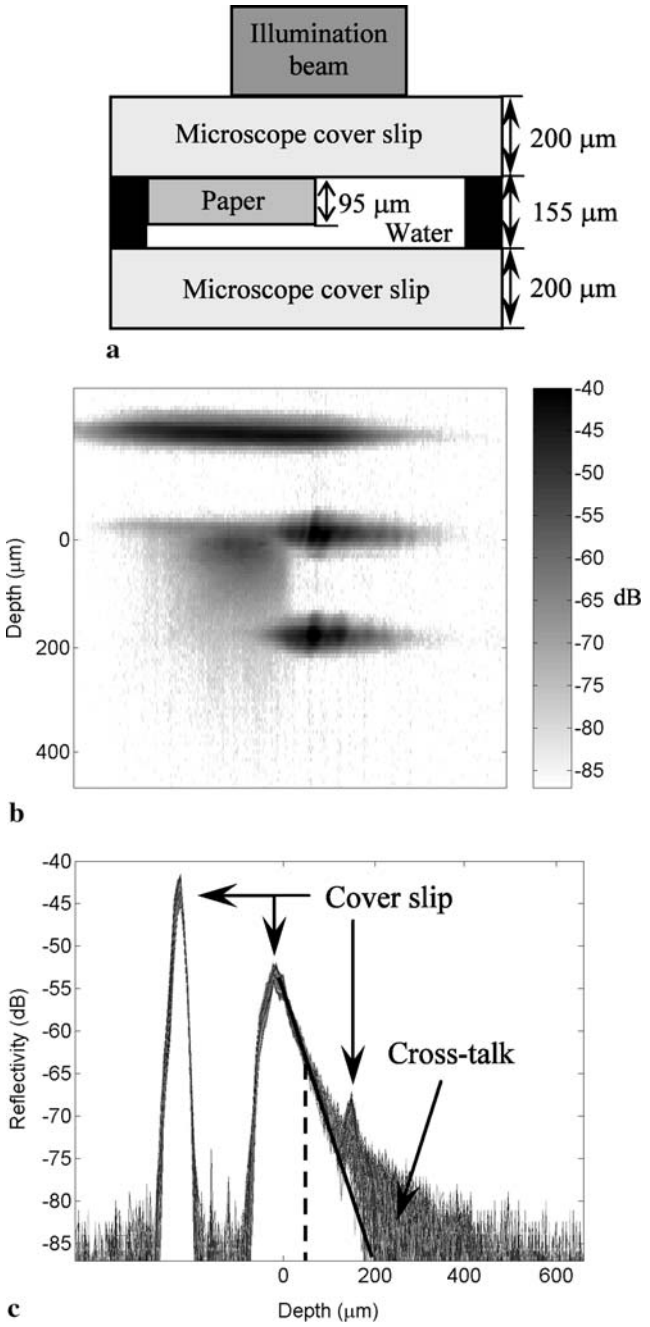

Fig. 5 (**a**) Schematic of diffuse target (paper). (**b**) *YZ* cross section selected from the holographic images of the diffuse target with a reduced extinction coefficient of 125 mm^{-1} in the holographic OCI system with a vibrating 5 degree diffuser. (**c**) Pseudo A-scans selected from the holographic images. The stretched exponential beyond the depth of the *dashed line* (50 µm) is multiple-scattering channel cross-talk. The depth in units of optical thickness at this point is 12.5 for the round-trip

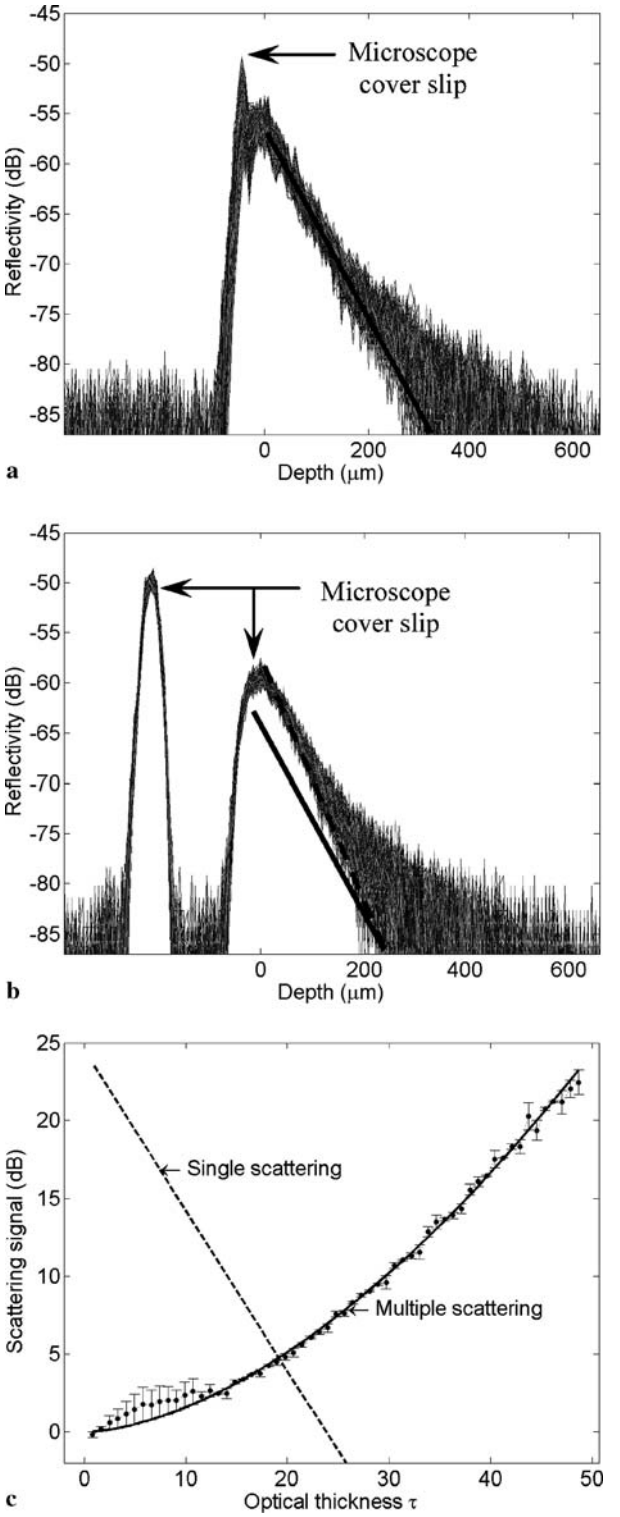

Fig. 6 Pseudo A-scans selected from the holographic images of 0.49-µm diameter polystyrene beads in water solution in the holographic OCI system with (**a**) no diffuser and (**b**) a vibrating diffuser. The reduced extinction coefficient of the uniform scattering medium was 55 mm^{-1}. The *solid line* in (**a**) and the *dashed line* in (**b**) are the slopes for single scattering. The *solid line* in (**b**) has the same slope as the *line* in (**a**). (**c**) Shows the contribution of single scattering photons (*dashed line*) and multiple-scattering photons (*solid line*) to the holographic images as a function of the optical thickness

data for no diffuser and for a vibrating 5 degree diffuser, respectively. The peak intensities in the figure show the surfaces of the microscope cover slip. Figure 6(a) shows no top cover slip because the top specular reflection is eliminated by the aperture at the image plane in Fig. 1. On the other

hand, for Fig. 6(b) the diffuser angle was within the numerical aperture of the collection optics, and hence the microscope cover slip surface is captured in the holograms. The collected light in the holographic OCI system with the vibrating diffuser was similar to that in the system with no diffuser, while the overall multiple-scattering channel cross-talk was reduced. The reduced multiple-scattering channel cross-talk can be evaluated by comparing the slopes of the pseudo A-scans between Figs. 6(a) and (b). The slope of the dashed line in Fig. 6(b) was increased by about 34% when compared with the slope of the solid line from Fig. 6(a). This demonstrates that multiply-scattered channel cross-talk can be reduced by use of the vibrating diffuser in the holographic OCI system.

Even though the channel cross-talk is reduced by the spatially scrambled illumination beam, the coherence gate still accepts non-image-bearing photons, as shown on the right side of the dashed line in Fig. 6(b). To quantify the contribution of multiply-scattered channel cross-talk to holographic images as a function of optical thickness, we averaged the reflectance at each depth from the data for Fig. 6(b). The numerical value corresponding to the solid line in Fig. 6(b) was subtracted from this averaged value. The residual values are the contribution of multiple-scattering channel cross-talk, shown by circles in Fig. 6(c) as a function of the optical thickness. The depth was converted to optical thickness using the reduced extinction coefficient of 55 mm^{-1}. The multiple-scattering channel cross-talk increases with depth faster than exponentially, reflecting the combinatorics of increasing phase space for increasing combinations of scattering events that match the path length of the coherence gate. The dashed line in Fig. 6(c) is the contribution of single scattering to holographic images. For this dashed line, the noise floor of -82 dB was subtracted from the solid line in Fig. 6(b). The crossing point of the solid line and the dashed line is at 19.2 optical thickness. At this crossing point, the contribution of single scattering photons is the same as for multiply-scattered photons. This demonstrates that the multiply-scattered photons in holographic OCI with a vibrating diffuser overwhelm the single scattering photons beyond the scattering depth of about 20 optical thickness. This cross-over is close to the result of an earlier study in time-gated transillumination imaging [14].

5 Channel cross-talk in multicellular tumor spheroids

We used rat osteogenic sarcoma tumor spheroids [39, 40] to investigate channel cross-talk in living tissue. Rat osteogenic sarcoma UMR-106 cells were cultured in Dulbecco's modified Eagles' medium in non-tissue-culture plastic dishes to create tumor spheroids. The non-tissue-culture plastic causes the tumor cells to form the spheroids in 7–10 days; the spheroids are then transferred to a rotating bioreactor where they are maintained in suspension. The spheroids were grown up to 1 mm in diameter and are thus large enough to simulate the thickness of different mammalian tissue. As tumor spheroids are cultured, they undergo cell apoptosis or necrosis in their center and so consist of an inner necrotic core and an outer shell with a 100- to 200-μm thickness of healthy cells [41].

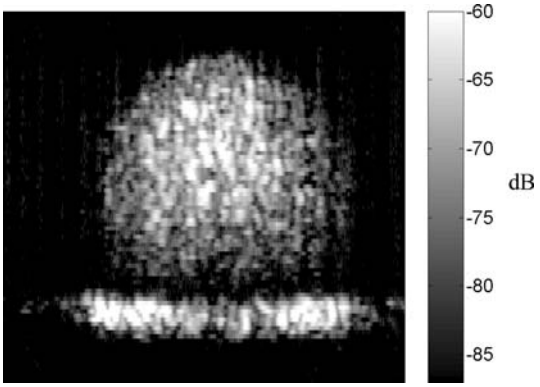

Fig. 7 YZ cross section from holographic images of a 400 μm diameter rat osteogenic tumor spheroid. The Petri dish reflection appears on the bottom. Note the circular shape of the tumor spheroid. Multiply-scattered light, if present, would appear beyond the Petri dish, but is not observed for this tissue type

We performed holographic optical coherence imaging on tumor spheroids to quantify the contribution of multiple-scattered light to the coherence-gated images. Holographic images of tumor spheroids were captured by the CCD camera using a depth step of 10 μm step. Figure 7 shows YZ cross sections from the holographic *en face* images of a 400 μm diameter tumor spheroid on a dB scale. For these data, we used no diffuser. The tumor spheroid was in growth medium on a Petri dish, which appears as the reflection at the bottom. The average reduced extinction coefficient of tumor spheroids was measured to be about 10 mm^{-1} with an anisotropy factor of $g = 0.9$, obtained using conventional forward light scattering methods. The optical thickness at a 400 μm depth using the 10 mm^{-1} reduced extinction coefficient is $\tau = 8$ for the round-trip. Eight optical thicknesses is much smaller than the cross-over point (about 20) of single scattering and multiple scattering (discussed in the previous section). This implies that the contribution of multiply-scattered photons to the holographic images of this small tumor is small, and multiply-scattered light will be weak in the holographic images. The image in Fig. 7 illustrates this reduced multiple scattering when compared with the image of the diffuse paper in Fig. 5(b). Note that the shape of the tumor spheroid is circular. Multiply-scattered light, if present, would appear beyond the Petri dish, but is not observed for this tissue type. This demonstration is supported by Fig. 8, which displays pseudo A-scans selected from holographic

images of the tumor spheroid in Fig. 7. The signal is reduced linearly from the top of the tumor spheroid to the Petri dish, and suddenly drops to the noise level beyond the Petri dish. If multiple scattering were strong, the multiply-scattered signal would appear beyond the Petri dish (as seen in Fig. 5(c) and in Figs. 6(a) and (b)).

Even though the multiply-scattered light contribution to the coherence-gated imaging is not readily apparent in the tissue within 8 optical thickness, the multiply-scattered light may still make a small contribution to the image. We approximated the contribution of multiple scattering to the image acquired at a selected depth by changing the light polarization. Multiple scattering scrambles the light polarization after a few high-angle scattering events, while single scattering does not appreciably change the light polarization. If only the crossed-polarization light is collected from the backscattered light, this would be proportional to the multiple-scattered light contribution to the coherence-gated image. The results of the crossed-polarization experiment are shown in Fig. 9 as pseudo A-scans. The holographic images for these pseudo A-scans were produced in the holographic OCI system using no diffuser. Only the co-polarized light was recorded on the hologram for the left figure, and only the cross-polarized light was recorded for the right figure. In Fig. 9(a), the tumor has a characteristic slope of reflectance versus depth that should be related to the reduced extinction coefficient for the tissue. In Fig. 9(b), when the oppositely polarized light is selected from the light scattered from the tumor, signals were captured, but the multiply-scattered light contribution is small. The maximum reflectance of the cross-polarized light was −75 dB at a depth of about 200 microns, compared with −65 dB for the co-polarized light from the same depth. The number of co-polarized photons in multiply-scattering light will be similar to the number of cross-polarized photons if the multiple scattering scrambles the light polarization randomly. This implies that the contribution of multiply-scattered light to holograms in Fig. 9(a) is similar to that in Fig. 9(b).

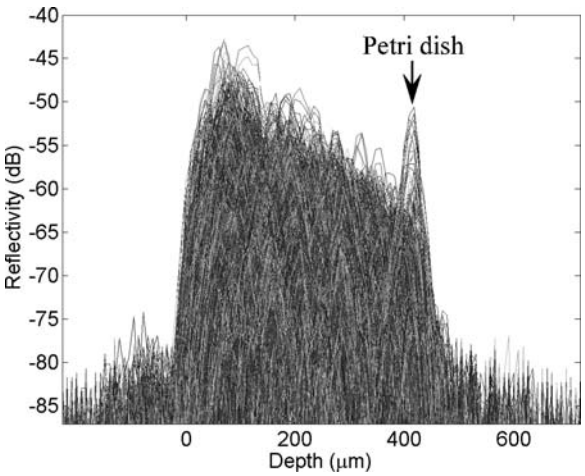

Fig. 8 Pseudo A-scans selected from holographic images of the tumor spheroid in Fig. 7. Note that the signal beyond the Petri dish drops suddenly to the noise level. The multiply-scattered light would appear beyond the Petri dish if multiple scattering were strong

The multiple-scattering contribution can be reduced by scrambling the spatial coherence of the illumination beam using a vibrating diffuser. This is shown in Fig. 10 for data taken without a diffuser and for data taken with a vibrating 0.5 degree diffuser. The slope of the dashed line in Fig. 10(b) is increased by 27% when compared with the slope of the solid line from Fig. 10(a). Therefore, the measured reduced extinction coefficient in holographic OCI is increased by 27% using a vibrating 0.5 degree diffuser. The increase in slope is caused by reduced contributions from multiple scattering at increasing depth.

6 Conclusion

This paper quantifies channel cross-talk in holographic OCI. The structural speckle and multiple-scattering channel cross-talk are both fundamental contributions to holographic optical coherence images. The structural speckle can be used to study the health of tissue through dynamic speckle or to obtain structure inside living tissue. We demonstrate that

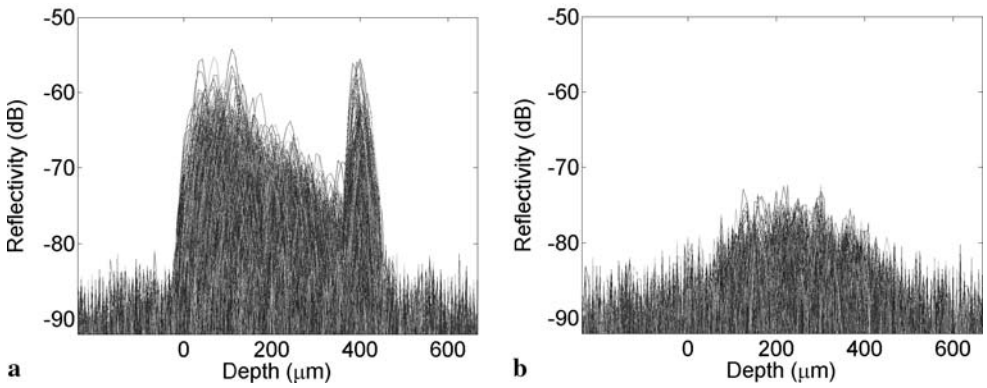

Fig. 9 The effect of crossed polarization on the coherence gating. The pseudo A-scans are selected from holographic images which were produced under (**a**) co-polarization and (**b**) cross-polarization. The crossed polarization provides a measure of multiple scattering

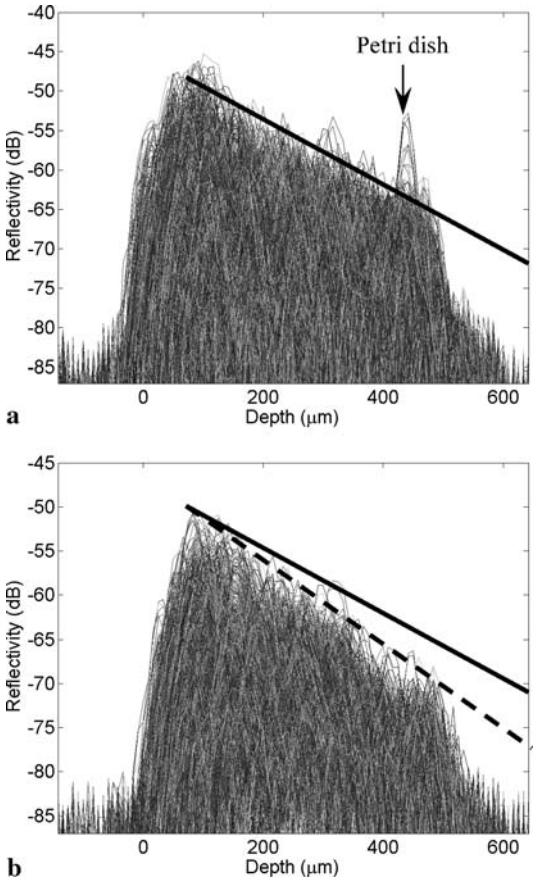

Fig. 10 Two pseudo A-scans of the same tumor (**a**) using no diffuser, and (**b**) with a vibrating 0.5 degree diffuser. Note the different slopes, with the larger slope in (**b**). The slope in (**b**) is increased by 27% when compared with the slope in (**a**)

the cross-over point for singly-scattered light and multiply-scattered light is about 15 to 20 optical thicknesses. This value was extracted through the slope of pseudo A-scans from the data of a model target. We demonstrated that multiple-scattering channel cross-talk is reduced by accepting only the co-polarized light in hologram recording and using a vibrating diffuser to scramble the spatial coherence of the illumination beam.

Acknowledgement This work was supported by the National Science Foundation under grant CBET-0756005.

References

1. V.V. Tuchin, Coherence-domain methods in tissue and cell optics. Laser Phys. **8**, 807–849 (1998)
2. J.G. Fujimoto, Optical coherence tomography for ultrahigh resolution in vivo imaging. Nat. Biotechnol. **21**, 1361–1367 (2003)
3. A.F. Fercher, W. Drexler, C.K. Hitzenberger, T. Lasser, Optical coherence tomography—principles and applications. Rep. Prog. Phys. **66**, 239–303 (2003)
4. D. Huang, E.A. Swanson, C.P. Lin, J.S. Schuman, W.G. Stinson, W. Chang, M.R. Hee, T. Flotte, K. Gregory, C.A. Puliafto, J.G. Fujimoto, Optical coherence tomography. Science **254**, 1178 (1991)
5. J.M. Schmitt, A. Knüttel, R.F. Bonner, Measurement of optical properties of biological tissues by low-coherence reflectometry. Appl. Opt **32**, 6032–6042 (1993)
6. E. Beaurepaire, A.C. Boccara, M. Lebec, L. Blanchot, H. Saint-Jalmes, Full-field optical coherence microscopy. Opt. Lett. **23**, 244 (1998)
7. A. Dubois, K. Grieve, G. Moneron, R. Lecaque, L. Vabre, C. Boccara, Ultrahigh-resolution full-field optical coherence tomography. Appl. Opt. **43**, 2874–2883 (2004)
8. S.C.W. Hyde, R. Jones, N.P. Barry, J.C. Dainty, P.M.W. French, K.M. Kwolek, D.D. Nolte, M.R. Melloch, Depth-resolved holography through turbid media using photorefraction. IEEE J. Sel. Top. Quantum Electron. **2**, 965 (1996)
9. R. Jones, M. Tziraki, P.M.W. French, K.M. Kwolek, D.D. Nolte, M.R. Melloch, Direct-to-video holographic 3-D imaging using photorefractive multiple quantum well devices. Opt. Express **2**, 438 (1998)
10. M. Tziraki, R. Jones, P.M.W. French, M.R. Melloch, D.D. Nolte, Photorefractive holography for imaging through turbid media using low coherence light. Appl. Phys. B **70**, 151 (2000)
11. C. Dunsby, P.M.W. French, Techniques for depth-resolved imaging through turbid media including coherence-gated imaging. J. Phys. D: Appl. Phys. **36**, R207–R227 (2003)
12. D.D. Nolte, T. Cubel, L.J. Pyrak-Nolte, M.R. Melloch, Adaptive beam combining and interferometry using photorefractive quantum wells. J. Opt. Soc. Am. B **18**, 195–205 (2001)
13. M. Tziraki, R. Jones, P. French, D. Nolte, M. Melloch, Short-coherence photorefractive holography in multiple-quantum-well devices using light-emitting diodes. Appl. Phys. Lett. **75**, 363–65 (1999)
14. D.D. Nolte, Semi-insulating semiconductor heterostructures: optoelectronic properties and applications. J. Appl. Phys. **85**, 6259 (1999)
15. R.M. Brubaker, Q.N. Wang, D.D. Nolte, M.R. Melloch, Nonlocal photorefractive response induced by intervalley electron scattering in semiconductors. Phys. Rev. Lett. **77**, 4249–52 (1996)
16. K.M. Kwolek, M.R. Melloch, D.D. Nolte, G.A. Brost, Diffractive quantum-well asymmetric Fabry–Perot: transverse-field photorefractive geometry. Appl. Phys. Lett. **67**, 736 (1995)
17. P. Yu, L. Peng, M. Mustata, J.J. Turek, M.R. Melloch, D.D. Nolte, Time-dependent speckle in holographic optical coherence imaging and the state of health of tumor tissue. Opt. Lett. **29**, 68–70 (2004)
18. P. Yu, M. Mustata, L.L. Peng, J.J. Turek, M.R. Melloch, P.M.W. French, D.D. Nolte, Holographic optical coherence imaging of rat osteogenic sarcoma tumor spheroids. Appl. Opt. **43**, 4862–4873 (2004)
19. P. Yu, M. Mustata, P.M.W. French, J.J. Turek, M.R. Melloch, D.D. Nolte, Holographic optical coherence imaging of tumor spheroids. Appl. Phys. Lett. **83**, 575 (2003)
20. K. Jeong, L. Peng, J.J. Turek, M.R. Melloch, D.D. Nolte, Fourier-domain holographic optical coherence imaging of tumor spheroids and mouse eye. Appl. Opt. **44**, 1798–1806 (2005)
21. K. Jeong, L.L. Peng, D.D. Nolte, M.R. Melloch, Fourier-domain holography in photorefractive quantum-well films. Appl. Opt. **43**, 3802–3811 (2004)
22. K. Jeong, J.J. Turek, M.R. Melloch, D.D. Nolte, Functional imaging in photorefractive tissue speckle holography. Opt. Commun. **281**, 1860–1869 (2008)
23. D.D. Steele, B.L. Volodin, O. Savina, B. Kippelen, N. Peyghambarian, H. Rockel, S.R. Marder, Transillumination imaging through scattering media by use of photorefractive polymers. Opt. Lett. **23**, 153–155 (1998)
24. R. Mahon, W.S. Rabinovich, M. Bashkansky, S.R. Bowman, K. Ikossi-Anastasiou, D.S. Katzer, Depth-gated imaging using lock-in holography. J. Opt. Soc. Am. B: Opt. Phys. **19**, 1685–1691 (2002)

25. E. Mecher, F. Gallego-Gomez, H. Tillmann, H.H. Horhold, J.C. Hummelen, K. Meerholz, Near-infrared sensitivity enhancement of photorefractive polymer composites by pre-illumination. Nature **418**, 959–964 (2002)
26. P. Dean, M.R. Dickinson, D.P. West, Full-field coherence-gated holographic imaging through scattering media using a photorefractive polymer composite device. Appl. Phys. Lett. **85**, 363–365 (2004)
27. G. Ramos-Ortiz, M. Cha, B. Kippelen, G.A. Walker, S. Barlow, S.R. Marder, Direct imaging through scattering media by use of efficient third-harmonic generation in organic materials. Opt. Lett. **29**, 2515–2517 (2004)
28. P. Dean, M.R. Dickinson, D.P. West, Depth-resolved holographic imaging through scattering media by use of a photorefractive polymer composite device in the near infrared. Opt. Lett. **30**, 1941–1943 (2005)
29. A. Kabir, A.M. Ajward, H.P. Wagner, Holographic imaging using the phase coherent photorefractive effect in ZnSe quantum wells. Appl. Phys. Lett. **93** (2008)
30. K. Jeong, J.J. Turek, D.D. Nolte, Fourier-domain digital holographic optical coherence imaging of living tissue. Appl. Opt. **46**, 4999–5008 (2007)
31. K. Jeong, J.J. Turek, D.D. Nolte, Imaging motility contrast in digital holography of tissue response to cytoskeletal anti-cancer drugs. Opt. Express **15**, 14057 (2007)
32. U. Schnars, W.P.O. Juptner, Digital recording and numerical reconstruction of holograms. Meas. Sci. Technol. **13**, R85–R101 (2002)
33. M.C. Potcoava, M.K. Kim, Optical tomography for biomedical applications by digital interference holography. Meas. Sci. Technol. **19** (2008)
34. S.G. Adie, T.R. Hillman, D.D. Sampson, Detection of multiple scattering in optical coherence tomography using the spatial distribution of Stokes vectors. Opt. Express **15**, 18033–18049 (2007)
35. B. Karamata, M. Leutenegger, M. Laubscher, S. Bourquin, T. Lasser, P. Lambelet, Multiple scattering in optical coherence tomography, II: experimental and theoretical investigation of cross talk in wide-field optical coherence tomography. J. Opt. Soc. Am. A: Opt. Image Sci. Vis. **22**, 1380–1388 (2005)
36. J.M. Schmitt, S.H. Xiang, K.M. Yung, Speckle in optical coherence tomography. J. Biomed. Opt. **4**, 95–105 (1999)
37. M.R. Hee, J.A. Izatt, J.M. Jacobson, J.G. Fujimoto, E.A. Swanson, Femtosecond transillumination optical coherence tomography. Opt. Lett. **18**, 950 (1993)
38. S. Balasubramanian, I. Lahiri, Y. Ding, M.R. Melloch, D.D. Nolte, Two-wave mixing dynamics and nonlinear hot-electron transport in transverse-geometry photorefractive quantum wells studied by moving gratings. Appl. Phys. B **68**, 863–9 (1999)
39. L.A. Kunz-Schughart, Multicellular tumor spheroids: intermediates between monolayer culture and in vivo tumor. Cell Biol. Int. **23**, 157–161 (1999)
40. M.T. Santini, G. Rainaldi, Three-dimensional spheroid model in tumor biology. Pathobiology **67**, 148–157 (1999)
41. M. Marusic, Z. Bajzer, J.P. Freyer, S. Vuk-Pavlovic, Analysis of growth of multicellular tumor spheroids by mathematical models. Cell Prolif. **27**, 73–94 (1994)